Vol 17 No 10, October 2008
1674-1056/2008/17(10)/3847-09

Chinese Physics B

© 2008 Chin. Phys. Soc.
and IOP Publishing Ltd

Numerical investigation of the deformation mechanism of a bubble or a drop rising or falling in another fluid*

Wang Han(王 含)[a], Zhang Zhen-Yu(张振宇)[b], Yang Yong-Ming(杨永明)[a]†, Hu Yüe(胡 越)[a], and Zhang Hui-Sheng(张慧生)[a]

[a] *Department of Mechanics and Engineering Science, Fudan University, Shanghai* 200433, *China*

[b] *Department of Mathematics, Shanghai University of Finance and Economics, Shanghai* 200433, *China*

(Received 4 February 2008; revised manuscript received 9 June 2008)

A numerical method for simulating the motion and deformation of an axisymmetric bubble or drop rising or falling in another infinite and initially stationary fluid is developed based on the volume of fluid (VOF) method in the frame of two incompressible and immiscible viscous fluids under the action of gravity, taking into consideration of surface tension effects. A comparison of the numerical results by this method with those by other works indicates the validity of the method. In the frame of inviscid and incompressible fluids without taking into consideration of surface tension effects, the mechanisms of the generation of the liquid jet and the transition from spherical shape to toroidal shape during the bubble or drop deformation, the increase of the ring diameter of the toroidal bubble or drop and the decrease of its cross-section area during its motion, and the effects of the density ratio of the two fluids on the deformation of the bubble or drop are analysed both theoretically and numerically.

Keywords: bubble, drop, buoyancy, deformation mechanism, VOF method
PACC: 6810

1. Introduction

The rising and falling of bubbles or drops in another fluid occur very often in nature and in engineering (e.g. chemical engineering). The study of the deformation mechanism during their buoyancy-driven motion will be helpful to both fluid mechanics and engineering. Because of the strong nonlinearity accompanied by their large deformations, it is difficult to study the mechanism by purely analytical methods. The study is mainly based on the experimental and numerical methods. Experimental method is the most direct and original way to find new phenomena and to explore the associated mechanisms. It is difficult for the experimental methods, however, to give the detailed velocity and pressure distributions of the flow field (these are important in the study) due to the limitations of measuring means or financial supports. Numerical methods, on the other hand, can give the detailed flow information.

Numerical methods for simulating the deformation of bubbles and drops can mainly be divided into two categories. One is the kind of boundary integral methods,[1,2] which only needs to arrange the grids on the interfaces of the fluids and thus reduces the dimensions of the problem by one so that the computational amounts are, compared to the other kind of methods mentioned below, reduced considerably. However, this kind of methods is difficult to simulate the topological changes such as the transition from single-connected domain to multi-connected domain, the merging and break of the bubbles and drops, etc. It is also difficult to model the viscous effects of the fluids for flows with moderate Reynolds numbers, and is not convenient to give the velocity and pressure distributions.

The other category is the kind of methods based on the full-flow-field solutions. This kind of methods can easily simulate the topological changes of the interfaces, model the viscous effects of the fluids, and give the detailed velocity and pressure distributions as a direct result of computations. Among these methods, level set methods[3−5] and volume-of-fluid (VOF) methods[4,6−8] are the strongest and most popularly used ones. Level set methods cannot ensure the mass-conservation. This drawback can be reduced by re-

*Project supported by the National Natural Science Foundation of China (Grant Nos 10672043 and 10272032).
†Corresponding author. E-mail: yangym@fudan.edu.cn

initialization technique,[9] but it is difficult to be eliminated completely. VOF methods can suffer from 'flotsam and jetsam', but the mass-conservation can be rigorously satisfied by them.

In the following cited experimental and numerical works the bubbles or drops are all initially spherical and the fluid around them is infinite and initially stationary. Reference [10] studied an air bubble rising in water and found that after the bubble rose a distance a liquid jet formed and developed below the lower surface of the bubble, and finally it impacted and penetrated the upper surface of the bubble and made the bubble toroidal. References [11] and [12] studied the buoyancy-driven motion of a bubble and a drop respectively through a quiescent liquid by finite difference methods based on the body-fitted coordinate transformations and found that as the Reynolds and Weber numbers were increased, steady-rising bubble solutions could not be obtained. Reference [13] studied the rise and distortion of a bubble by boundary integral method and found that when the Weber number was sufficiently large, the bottom surface would collide with its upper surface, causing the formation of a toroidal bubble. But the computation was stopped just before jet impact, then restarted from a toroidal bubble with an assumed shape and under initial conditions, and its results did not give detailed description of the toroidal bubble. Reference [14] simulated the transition of a spherical rising bubble in a liquid to a toroidal one by level set method and found that the results were in good agreement with those in Ref.[13] before jet impact. Reference [15] modelled a rising bubble in a liquid by level set method and gave the velocity and pressure distributions at the time just before jet impact to illustrate the formation of the toroidal bubble. All of the above works did not give the mechanism analysis of the bubble and drop deformations.

The purpose of this paper is to investigate numerically the deformation mechanism of an initially spherical bubble or drop during their buoyancy-driven motion (rising or falling) in another infinite and initially stationary fluid by VOF method. Thus the induced flow must be axisymmetric. The governing equations including viscosity and surface tension effects, and the associated numerical methods are given. But the deformation pattern of the bubble or drop is governed by many dimensionless parameters such as density and viscosity ratios of the fluids, Reynolds number and Weber number, etc. In order to understand clearly the deformation mechanism it is necessary to study the effects of individual parameters separately. As a first step we will study large bubbles or drops. In this case the Reynolds number Re and the Weber number We are large (e.g. for water and air at 20°C, when the radius of the bubble or drop is greater than or equal to 2 cm, we have $We \geq 53.8$ and water property based $Re \geq 8820$). Thus surface tension effects can be neglected. Due to the adaptive deformation of the interface, flow separation is not easy to occur.[16] Therefore, for the high Reynolds number flow, viscosity effects are confined within the very thin boundary layer. Thus as a proper approximation, the flow can be assumed inviscid. Because the flow velocity is much lower than the speed of sound, the fluids at both sides of the interface can be assumed incompressible. Note that the only body force is the gravity which is potential and that the fluids are initially stationary, so by Kelvin theorem the flow will be irrotational all the time. In this case the only dimensionless parameter which affects the flow pattern is the density ratio of the two fluids.

2. Governing equations and numerical methods

We study the buoyancy-driven motion of an axisymmetric bubble or drop with surface S in an infinite and initially stationary fluid. Let the fluids outside and inside S be marked by 1 and 2 respectively. The two fluids are assumed to be immiscible and incompressible. Let ρ and μ be the fluid density and viscosity respectively, and C be the ratio of the volume of fluid 1 in a cell to the volume of the cell (C is called colour function). Let l_0, $u_0 = \sqrt{gl_0}$, $t_0 = l_0/u_0$, $p_0 = \rho_1 u_0^2$, ρ_1 and μ_1 be the reference quantities of length, velocity, time, pressure, density and viscosity respectively, and introduce the following dimensionless quantities $\bar{r} = r/l_0$, $\bar{z} = z/l_0$, $\bar{t} = t/t_0$, $\bar{u} = u/u_0$, $\bar{v} = v/u_0$, $\bar{p} = p/p_0$, $\bar{\rho} = \rho/\rho_1$, $\bar{\mu} = \mu/\mu_1$, then we can gain the dimensionless governing equations for the flow problem. In the above expressions r and z are respectively the radial and axial coordinates, t is the time variable, u and v are respectively the r- and z-components of the velocity, p is the pressure, g is the acceleration due to gravity, σ is the surface tension between fluids 1 and 2, α is the total curvature of S, $\delta(S)$ is the Dirac δ-function with sources distributed on S, and n_r and n_z are respectively the r- and z-

components of the unit normal of S. If we drop the sign '–' over any dimensionless quantity, then the dimensionless governing equations are

$$\frac{1}{r}\frac{\partial(ru)}{\partial r}+\frac{\partial v}{\partial z}=0, \tag{1}$$

$$\begin{aligned}&\frac{\partial u}{\partial t}+\frac{1}{r}\frac{\partial(ru^2)}{\partial r}+\frac{\partial(uv)}{\partial z}\\ =&\frac{1}{\mathrm{We}\rho}\alpha\delta(S)n_r-\frac{1}{\rho}\frac{\partial p}{\partial r}\\ &+\frac{1}{\mathrm{Re}\rho}\left\{\frac{1}{r}\frac{\partial}{\partial r}\left(2\mu r\frac{\partial u}{\partial r}\right)\right.\\ &\left.+\frac{\partial}{\partial z}\left[\mu\left(\frac{\partial u}{\partial z}+\frac{\partial v}{\partial r}\right)\right]-\frac{2\mu u}{r^2}\right\},\end{aligned} \tag{2}$$

$$\begin{aligned}&\frac{\partial v}{\partial t}+\frac{1}{r}\frac{\partial(ruv)}{\partial r}+\frac{\partial(v^2)}{\partial z}\\ =&\frac{1}{\mathrm{We}\rho}\alpha\delta(S)n_z-\frac{1}{\mathrm{Fr}}-\frac{1}{\rho}\frac{\partial p}{\partial z}\\ &+\frac{1}{\mathrm{Re}\rho}\left\{\frac{1}{r}\frac{\partial}{\partial r}\left[r\mu\left(\frac{\partial u}{\partial z}+\frac{\partial v}{\partial r}\right)\right]\right.\\ &\left.+\frac{\partial}{\partial z}\left(2\mu\frac{\partial v}{\partial z}\right)\right\},\end{aligned} \tag{3}$$

$$\frac{\partial C}{\partial t}+u\frac{\partial C}{\partial r}+v\frac{\partial C}{\partial z}=0, \tag{4}$$

$$\rho=\lambda+C(1-\lambda), \tag{5}$$

$$\mu=\beta+C(1-\beta), \tag{6}$$

where the dimensionless parameters λ, β, Fr, Re and We are respectively the density ratio, viscosity ratio, Froude number, Reynolds number and Weber number, which are defined as

$$\begin{aligned}&\lambda=\frac{\rho_2}{\rho_1},\quad \beta=\frac{\mu_2}{\mu_1},\quad \mathrm{Fr}=\frac{u_0^2}{gl_0},\\ &\mathrm{Re}=\frac{\rho_1u_0l_0}{\mu_1},\quad \mathrm{We}=\frac{\rho_1u_0^2l_0}{\sigma}.\end{aligned} \tag{7}$$

Because in this paper we take $u_0=\sqrt{gl_0}$, we always have $Fr=1$ and $We=\rho_1gl_0^2/\sigma$ (in this case We is called Bond number B). When $\lambda>1$ we call fluid 2 a drop and when $\lambda<1$ we call fluid 2 a bubble although it is not a real bubble when the condition of $\lambda\ll1$ is not satisfied.

At the infinite boundary the velocity is zero and the pressure is the stationary fluid pressure. In the following computations, by use of the axisymmetric property of the fluid flow, the grid points at the symmetric axis can be treated as inner grid points.

As shown in Fig.1, in the longitudinal section the flow field is discretized into equal rectangles with side lengths Δr and Δz and with the symmetric axis passing through the centres of the innermost rectangles.

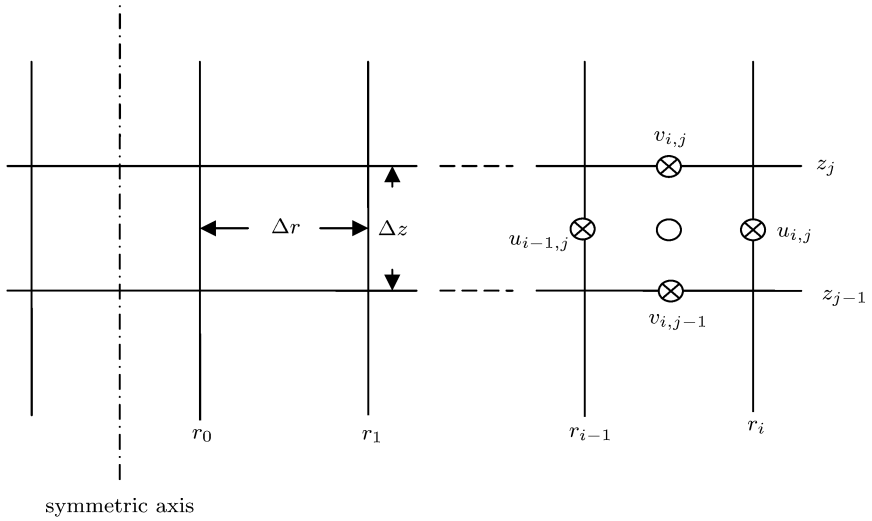


Fig.1. The discretization of the flow field.

In this paper a staggered grid system is used. In an (i,j) cell, the grid variables $\rho_{i,j}$, $p_{i,j}$, $\mu_{i,j}$ and $C_{i,j}$ are defined at the cell centre, $u_{i,j}$ is defined at the centre of its right side, and $v_{i,j}$ is defined at the centre of its top side. The discretization of Eqs.(5) and (6) is straightforward,

$$\rho_{i,j} = \lambda + (1-\lambda)C_{i,j}, \tag{8}$$

$$\mu_{i,j} = \beta + (1-\beta)C_{i,j}, \tag{9}$$

In this paper the interface in a cell is reconstructed by the piecewise linear interface calculation (PLIC) method. In the interface reconstruction, the unit normal is so chosen that it makes the constructed interface keep exactly the same $C_{i,j}$ in the concerned cell (i, j) and makes the error function reach its minimum, where the error function is the weighted sum of $(\tilde{C}_{i',j'} - C_{i',j'})^2 (i-1 \le i' \le i+1,\ j-1 \le j' \le j+1)$ and the sign '$\sim$' indicates the colour function obtained by extending the reconstructed interface to the neighbour cells. The weighted factors are proportional to the reciprocal of the squares of the distances between the cell concerned and its neighbour cells.

The discretization of the surface tension terms in Eqs.(2) and (3) is implemented by the continuum surface force (CSF) method,[17] and the method in Ref.[18] is extended to the axisymmetric problems to avoid the spurious currents induced by the conventional CSF method.

In the discretization of the momentum equations (2) and (3), the forward time differences, the centred spatial differences for pressure and viscosity terms, and the second-order TVD (total variation diminishing) differences for the advection terms are used. Let the superscript 'n' indicate the variable at nth time step, then the discretization of Eqs.(2) and (3) are respectively (the superscript 'n' is omitted)

$$\begin{aligned}
&(u_{i,j}^{n+1} - u_{i,j})/\Delta t + (r_{i+\frac{1}{2}} \bar{u}_{i+\frac{1}{2},j} \tilde{u}_{i+\frac{1}{2},j} - r_{i-\frac{1}{2}} \bar{u}_{i-\frac{1}{2},j} \tilde{u}_{i-\frac{1}{2},j})/(r_i \Delta r) \\
&+ (\bar{v}_{i+\frac{1}{2},j} \tilde{u}_{i,j+\frac{1}{2}} - \bar{v}_{i+\frac{1}{2},j-1} \tilde{u}_{i,j-\frac{1}{2}})/(\Delta z) \\
=&\mathrm{F}_{i,j}/(\mathrm{We}\rho_{i+\frac{1}{2},j}) - (p_{i+1,j}^{n+1} - p_{i,j}^{n+1})/(\rho_{i+\frac{1}{2},j}\Delta r) \\
&+ \{2[\mu_{i+1,j} r_{i+\frac{1}{2}} (u_{i+1,j} - u_{i,j}) - \mu_{i,j} r_{i-\frac{1}{2}} (u_{i,j} - u_{i-1,j})]/(r_i \Delta r^2) \\
&+ [\mu_{i+\frac{1}{2},j+\frac{1}{2}} ((u_{i,j+1} - u_{i,j})/\Delta z + (v_{i+1,j} - v_{i,j})/\Delta r) \\
&- \mu_{i+\frac{1}{2},j-\frac{1}{2}} ((u_{i,j} - u_{i,j-1})/\Delta z + (v_{i+1,j-1} - v_{i,j-1})/\Delta r)]/\Delta z \\
&- 2\mu_{i+\frac{1}{2},j} u_{i,j}/r_i^2\}/(\mathrm{Re}\rho_{i+\frac{1}{2},j}),
\end{aligned} \tag{10}$$

and

$$\begin{aligned}
&(v_{i,j}^{n+1} - v_{i,j})/\Delta t + (r_i \bar{u}_{i,j+\frac{1}{2}} \tilde{v}_{i+\frac{1}{2},j} - r_{i-1} \bar{u}_{i-1,j+\frac{1}{2}} \tilde{v}_{i-\frac{1}{2},j})/(r_{i-\frac{1}{2}} \Delta r) \\
&+ (\bar{v}_{i,j+\frac{1}{2}} \tilde{v}_{i,j+\frac{1}{2}} - \bar{v}_{i,j-\frac{1}{2}} \tilde{v}_{i,j-\frac{1}{2}})/(\Delta z) \\
=&G_{i,j}/(\mathrm{We}\rho_{i,j+\frac{1}{2}}) - \frac{1}{\mathrm{Fr}} - (p_{i,j+1}^{n+1} - p_{i,j}^{n+1})/(\rho_{i,j+\frac{1}{2}}\Delta z) \\
&+ \{[\mu_{i+\frac{1}{2},j+\frac{1}{2}} r_i ((u_{i,j+1} - u_{i,j})/\Delta z + (v_{i+1,j} - v_{i,j})/\Delta r) \\
&- \mu_{i-\frac{1}{2},j+\frac{1}{2}} r_{i-1} ((u_{i-1,j+1} - u_{i-1,j})/\Delta z + (v_{i,j} - v_{i-1,j})/\Delta r)]/(r_{i-\frac{1}{2}} \Delta r) \\
&+ 2[\mu_{i,j+1}(v_{i,j+1} - v_{i,j}) - \mu_{i,j}(v_{i,j} - v_{i,j-1})]/\Delta z^2\}/(\mathrm{Re}\rho_{i,j+\frac{1}{2}}),
\end{aligned} \tag{11}$$

where $F_{i,j}$ and $G_{i,j}$ are respectively the r- and z- components of the surface tension force computed by the CSF method mentioned above; and $r_{i+\frac{1}{2}} = r_i + \Delta r/2$, $\bar{u}_{i+\frac{1}{2},j} = (u_{i,j} + u_{i+1,j})/2$, $\bar{u}_{i,j+\frac{1}{2}} = (u_{i,j} + u_{i,j+1})/2$, $\bar{v}_{i+\frac{1}{2},j} = (v_{i,j} + v_{i+1,j})/2$, $\bar{v}_{i,j+\frac{1}{2}} = (v_{i,j} + v_{i,j+1})/2$. $\tilde{u}_{i+\frac{1}{2},j}$, $\tilde{u}_{i,j+\frac{1}{2}}$, $\tilde{v}_{i+\frac{1}{2},j}$ and $\tilde{v}_{i,j+\frac{1}{2}}$ are obtained by the second order TVD scheme with minmod limiter, and with $\bar{u}_{i+\frac{1}{2},j}$, $\bar{v}_{i+\frac{1}{2},j}$, $\bar{u}_{i,j+\frac{1}{2}}$ and $\bar{v}_{i,j+\frac{1}{2}}$ respectively as their boundary values, where for real numbers a and b, the function minmod (a, b) is defined as

$$\mathrm{minmod}(a,b) = \begin{cases} \mathrm{sign}(a)\min(|a|,|b|), & \text{when } ab > 0; \\ 0, & \text{otherwise.} \end{cases}$$

It was found that if we simply use the formulas $\rho_{i+\frac{1}{2},j} = (\rho_{i,j} + \rho_{i+1,j})/2$, $\rho_{i,j+\frac{1}{2}} = (\rho_{i,j} + \rho_{i,j+1})/2$, $\mu_{i+\frac{1}{2},j+\frac{1}{2}} = (\mu_{i,j} + \mu_{i+1,j} + \mu_{i,j+1} + \mu_{i+1,j+1})/4$, etc.,

the numerical simulation would be inaccurate when the difference between the two fluid densities or viscosities was large (e.g. for water and air). In this paper, we have $C_{i+\frac{1}{2},j}$, $C_{i,j+\frac{1}{2}}$ and $C_{i+\frac{1}{2},j+\frac{1}{2}}$ based on the information of the reconstructed interface in the four quarters of a cell and then compute $\rho_{i+\frac{1}{2},j}$, $\rho_{i,j+\frac{1}{2}}$, $\mu_{i+\frac{1}{2},j}$, $\mu_{i,j+\frac{1}{2}}$, $\mu_{i+\frac{1}{2},j+\frac{1}{2}}$ by Eqs.(5) and (6), which making the numerical simulation much more accurate. When $r = 0$ the left hand side of Eq.(3) reduces to

$$\frac{\partial v}{\partial t} + \frac{1}{2}\frac{\partial (v^2)}{\partial z},$$

which is discretized by

$$\frac{v_{i,j}^{n+1} - v_{i,j}}{\Delta t} + \frac{\bar{v}_{i,j+\frac{1}{2}}\tilde{v}_{i,j+\frac{1}{2}} - \bar{v}_{i,j-\frac{1}{2}}\tilde{v}_{i,j-\frac{1}{2}}}{2\Delta z}.$$

The discretization of Eq.(1) is expressed as

$$\frac{r_i u_{i,j}^{n+1} - r_{i-1}u_{i-1,j}^{n+1}}{r_{i-\frac{1}{2}}\Delta r} + \frac{v_{i,j}^{n+1} - v_{i,j-1}^{n+1}}{\Delta z} = 0. \tag{12}$$

When $r = 0$, Eq.(1) reduces to

$$2\frac{\partial u}{\partial r} + \frac{\partial v}{\partial z} = 0,$$

which is discretized by

$$4\frac{u_{0,j}^{n+1}}{\Delta r} + \frac{v_{0,j}^{n+1} - v_{0,j-1}^{n+1}}{\Delta z} = 0. \tag{13}$$

From Eqs.(10) and (11) we can obtain

$$u_{i,j}^{n+1} = a_{i,j}^{(1)}(p_{i+1,j}^{n+1} - p_{i,j}^{n+1}) + a_{i,j}^{(2)}, \tag{14}$$

$$v_{i,j}^{n+1} = a_{i,j}^{(3)}(p_{i,j+1}^{n+1} - p_{i,j}^{n+1}) + a_{i,j}^{(4)}, \tag{15}$$

where $a_{i,j}^{(k)}$ $(k = 1, 2, 3, 4)$ are known quantities at the nth time step. Substituting Eqs.(14) and (15) into Eqs.(12) and (13), we obtain the pressure equation

$$\begin{aligned} p_{i,j}^{n+1} =& b_{i,j}^{(1)}p_{i-1,j}^{n+1} + b_{i,j}^{(2)}p_{i+1,j}^{n+1} + b_{i,j}^{(3)}p_{i,j-1}^{n+1} \\ &+ b_{i,j}^{(4)}p_{i,j+1}^{n+1} + b_{i,j}^{(5)}, \end{aligned} \tag{16}$$

where $b_{i,j}^{(k)}$ $(k = 1, 2, 3, 4, 5)$ are known quantities at the nth time step. The pressure equation is solved numerically by the successive over relaxation (SOR) iteration method.

3. Numerical results

Now we study the buoyancy-driven motion of an initially spherical bubble or drop in another infinite and initially stationary fluid. In the non-dimensionalization, the reference length and velocity are taken to be R, the radius of the bubble or drop at $t = 0$, and $\sqrt{gR}$ respectively. Therefore, in the dimensionless system the radius of the bubble or drop at $t = 0$ is always 1, and the Froude number Fr is also always 1. In this paper, all of the numerical results are in dimensionless form.

To solve our flow problem for an infinite fluid, it is necessary to truncate the flow field to finite: $0 \le r \le r_{\max}$ and $z_l \le z \le z_u$. Numerical experiments with $\Delta r = \Delta z = 0.1$ show that when $r_{\max} \ge 3$ and d_l, d_u, the distances from the bubble or drop to z_l, z_u, are greater than or equal to 2, the numerical

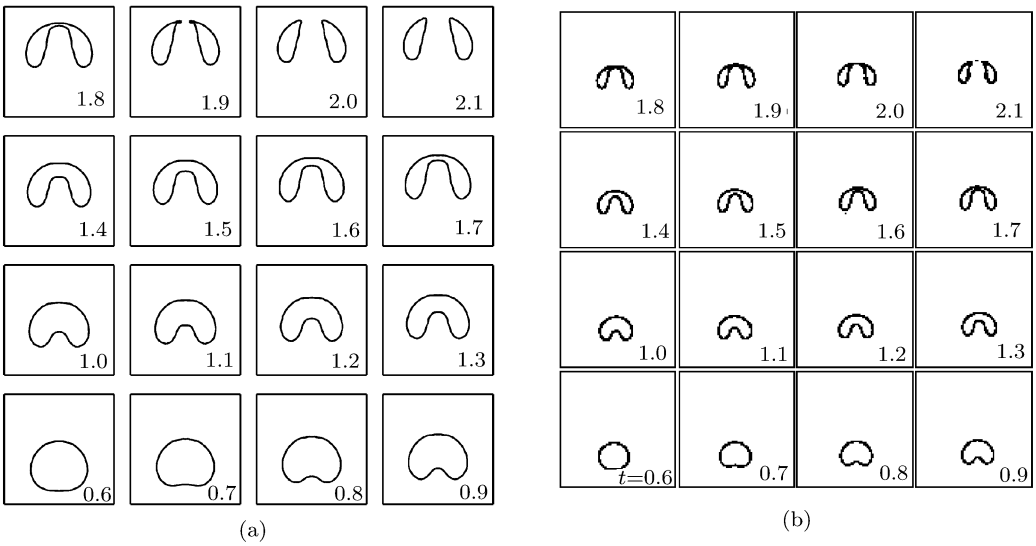


Fig.2. Evolution of an initially spherical gas bubble in a liquid with $\lambda = 0.001$, $\mathrm{Re} = \infty$, $\mathrm{We} = 10$ and $\mathrm{Fr} = 1$. (a) Result of this work. (b) Result taken from Fig.10 in Ref.[14].

results for the evolution of the bubble or drop only have small differences for different $r_{\max}$, z_l and z_u. In the computations in this paper we take $r_{\max} = 8$ and let z_l and z_u have suitable values so that $d_l \geq 7$ and $d_u \geq 7$ are ensured during the evolution of the bubble or drop. Numerical experiments also show that the numerical results with $\Delta r = \Delta z = 0.1$ and those with $\Delta r = \Delta z = 0.2$ have distinguishable differences, but the numerical results with $\Delta r = \Delta z = 0.1$ and those with $\Delta r = \Delta z = 0.05$ only have small differences. Thus in the computations, we take $\Delta r = \Delta z = 0.1$. In all of the computations, $\Delta t = 0.001$ is used.

For the case of $\lambda = 0.001$, $\mathrm{Re} = \infty$, $\mathrm{We} = 10$ and $\mathrm{Fr} = 1$, Fig.2(a) gives the evolution of an initially spherical gas bubble in a liquid by our method. Figure 2(b) shows the corresponding result taken from Fig.10 in Ref.[14] by level set method. Very good agreement between our result and the result in Ref.[14] is achieved, which shows the correctness of our method.

In what follows we study numerically the deformation mechanism of a bubble or drop during its buoyancy-driven motion in the frame of inviscid fluids without taking into consideration of surface tension effects. First we investigate a gas bubble rising in an infinite liquid. In this case the density ratio $\lambda(\approx 0.001)$ is very small. Figure 3 shows the evolution of an initially spherical gas bubble in a liquid with $\lambda = 0.001$, $\mathrm{Re} = \infty$, $\mathrm{We} = \infty$ and $\mathrm{Fr} = 1$. It can be seen that after the bubble rises for a moment, its bottom becomes flat and then concave, and then a large upward liquid jet forms and develops. Then a small downward liquid jet begins to form at the top of the bubble. The two liquid jets continuously develop and finally collide with each other and merge into a toroidal bubble. The toroidal bubble quickly splits at its top into a large toroidal bubble (at lower position) and a very small one (at upper position). As pointed out in Ref.[9], the mechanism of the generation of the very small toroidal bubble may be that when the two liquid jets collide with each other, the larger one carries a thin gas layer into the upper liquid which subsequently dissipates into small bubbles. During the development of the two toroidal bubbles, their diameters become larger and larger, and the areas of their cross sections become smaller and smaller.

Now we analyse the mechanism of the formation of the liquid jets. First we note that the contribution of the stationary fluid pressure p_{st} will cause the rising motion of the centroid of the bubble and thus the contribution of $p_{\mathrm{df}} = p - p_{\mathrm{st}}$ will cause the bubble to deform (we set $p_{\mathrm{df}} = 0$ at the centroid of the bubble). If we follow the rising bubble, we will see the flow around the bubble with the opposite of the velocity of the bubble centroid as the velocity at infinite. The flow in front of the bubble is blocked by the bubble and the flow in rear of the bubble collides with each other and is seriously blocked there. By Bernoulli's theorem, a large maximum of p_{df} will be generated somewhere behind and near the bubble, and a smaller maximum of p_{df} will be generated somewhere ahead of and near the bubble, which will cause large gradients of p_{df} near the two maximum points, but the gradient caused by the latter will be much smaller than that caused by the former. Because of the much lower density of the gas in the bubble, the large gradient of p_{df} will push the liquid near the bubble to move with a much larger acceleration and in turn a larger velocity than the other parts of the liquid around the maximum point; and this causes the liquid jet to form. Of course, the liquid jet behind the bubble must be much larger and stronger than that in front of the bubble.

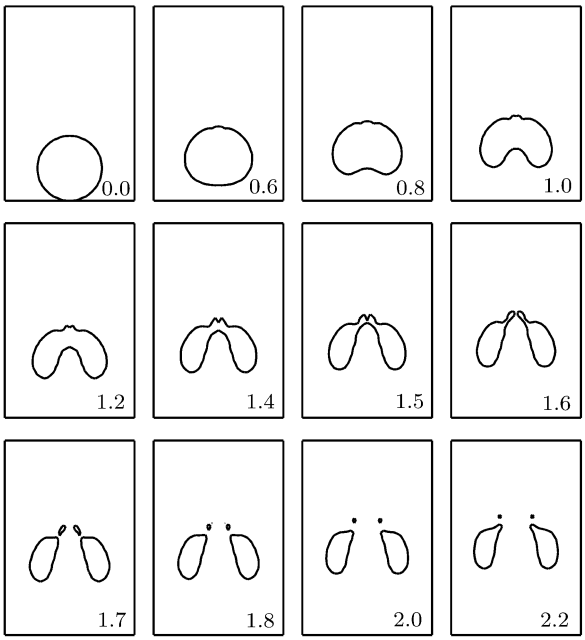


Fig.3. The evolution of a gas bubble in liquid with $\lambda = 0.001$, $\mathrm{Re} = \infty$, $\mathrm{We} = \infty$ and $\mathrm{Fr} = 1$.

For the case indicated in Figs.3, Figs.4(a) and 4(b) give respectively the pressure distribution of p_{df} and the velocity distribution at $t = 0.8$. It can be seen from Fig.4(a) that there are two maximum points of p_{df}: one is behind the bubble and the other is in front of it. Near the maximum points the gradient of p_{df} is large, but the gradient of p_{df} near the maximum point behind the bubble is much larger than that near the

maximum point in front of the bubble. Note that the isobaric lines of $p_{\rm df}$ in the bubble are horizontal parallels in equal distances, indicating that the pressure p in the bubble is almost a constant. It can be seen from Fig.4(b) that the flow velocity behind the bubble and that in front of the bubble are respectively greater and less than that at the centroid of the bubble. This causes the collision of the two jets ultimately.

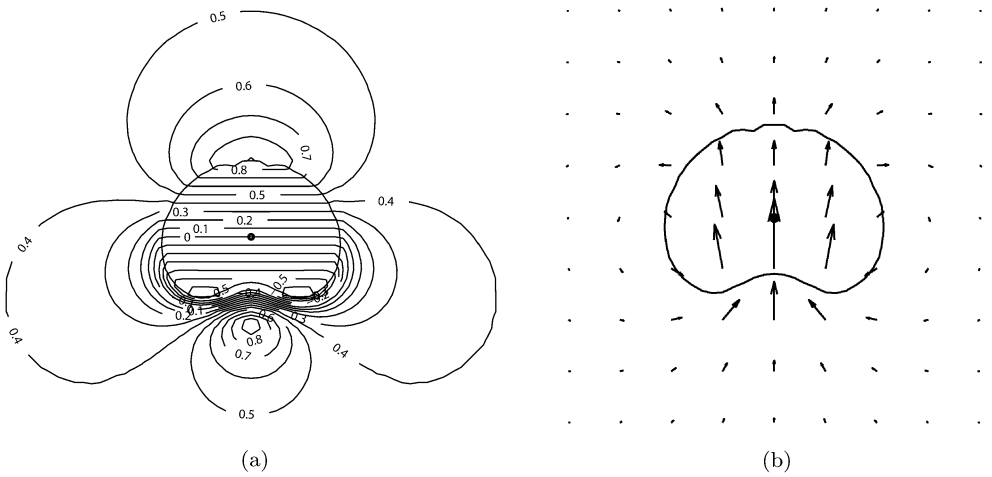


Fig.4. The pressure distribution of $p_{\rm df}$ and the velocity distribution at $t = 0.8$ for the case indicated in Fig.3. (a) Pressure distribution of $p_{\rm df}$. (b) Velocity distribution.

For the case indicated in Fig.3, Fig.5 gives the velocity distribution of the flow at $t = 1.8$. It can be seen that there is a circulation around the toroidal bubble, with an upward liquid flow in the ring and downward liquid flow outside of it. By Joukovsky theorem there exists an outward lift acting on the toroidal bubble, which causes it to move outward and its section area to decrease in order to keep the conservation of its volume.

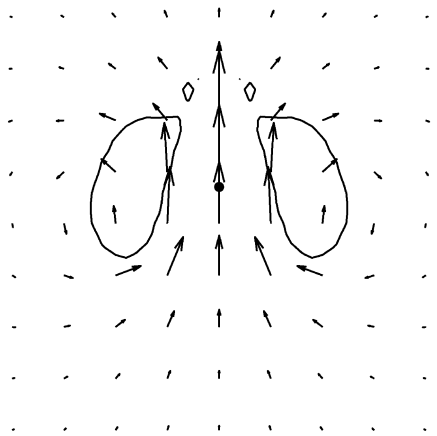


Fig.5. The velocity distribution of the flow at $t = 1.8$ for the case indicated in Fig.3.

Figure 6 shows the evolution of a bubble with $\lambda = 0.1$, Re $= \infty$, We $= \infty$ and Fr $= 1$. A rising water drop in mercury is close to this case. It can be seen that the evolution of the bubble shape is similar to that shown in Fig.3 because in this case the density of fluid 2 is still much smaller than that of fluid 1. Therefore the mechanisms of the generation of the liquid jet and the formation of the toroidal bubble are also similar to those in the case shown in Fig.3. However, the evolution is much slower than that in Fig.3. This is because the resistance to the deformation of the bubble is, compared to the case in Fig.3, much larger due to the larger value of the density ratio λ. Besides, the liquid jet is wider than that in Fig.3.

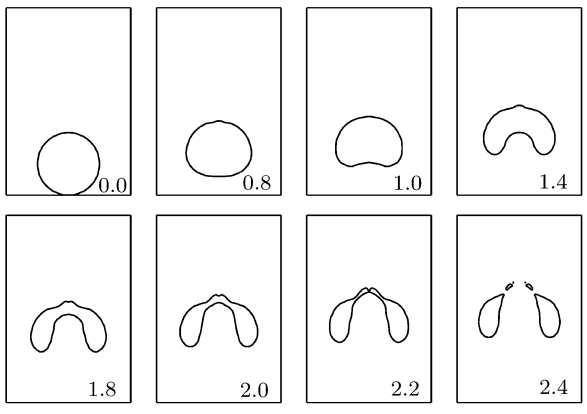


Fig.6. The evolution of a bubble with $\lambda = 0.1$, Re $= \infty$, We $= \infty$ and Fr $= 1$.

Figure 7 shows the evolution of a bubble with $\lambda = 0.8$, Re $= \infty$, We $= \infty$ and Fr $= 1$. A rising oil drop in water is close to this case. It can be seen that the evolution is much slower than that shown in Fig.6 because the resistance to the deformation of the bubble is much larger than that in the case in Fig.6 due to

the much larger value of the density ratio λ. There is also a liquid jet behind the bubble, but there is not any liquid jet in front of the bubble. The jet is much wider than that in Fig.6. When the jet advances forward for some time, its head begins to develop sideward and forward simultaneously. The continuous development of the jet makes the bubble like an umbrella with an earlobe-like edge. Finally the bubble splits into an umbrella-like bubble, a toroidal bubble with a nearly round cross-section and a small toroidal bubble with a thin cross-section.

For the case indicated in Fig.7, Fig.8 gives the pressure distribution of $p_{\rm df}$ at $t = 4$. It can be seen that there is a maximum point in rear of the bubble, but the gradient of $p_{\rm df}$ near the maximum point is much smaller than that in Fig.4(a). The isobaric lines of $p_{\rm df}$ in the bubble are no longer horizontal parallels, indicating that the flow in the bubble is more important than that in the case in Fig.3. Note that there is also a maximum point at the top of the bubble. Near the maximum point the gradient of $p_{\rm df}$ is not large enough to generate a liquid jet in front of the bubble.

Figure 9 shows the evolution of a drop with $\lambda = 1.25$, $\mathrm{Re} = \infty$, $\mathrm{We} = \infty$ and $\mathrm{Fr} = 1$. A falling water drop in oil is close to this case. It can be seen that the drop shape looks like the upside-down of the bubble shape in Fig.7, but the shape evolution is a little slower than that in Fig.7, because the resistance to the deformation of the drop is larger than that of the bubble due to the larger density in the drop.

For the case shown in Fig.9, Fig.10 gives the pressure distribution of $p_{\rm df}$ at $t = 4$. It can be seen that in rear of the drop there is a maximum point induced by the collision of the flow around the drop. Near the maximum point the gradient of $p_{\rm df}$ is large, which will

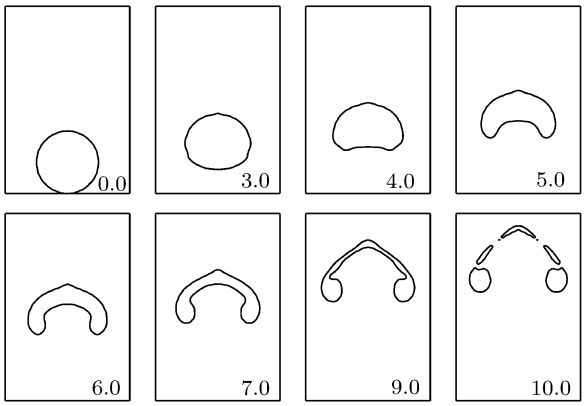


Fig.7. The evolution of a bubble with $\lambda = 0.8$, $\mathrm{Re} = \infty$, $\mathrm{We} = \infty$ and $\mathrm{Fr} = 1$.

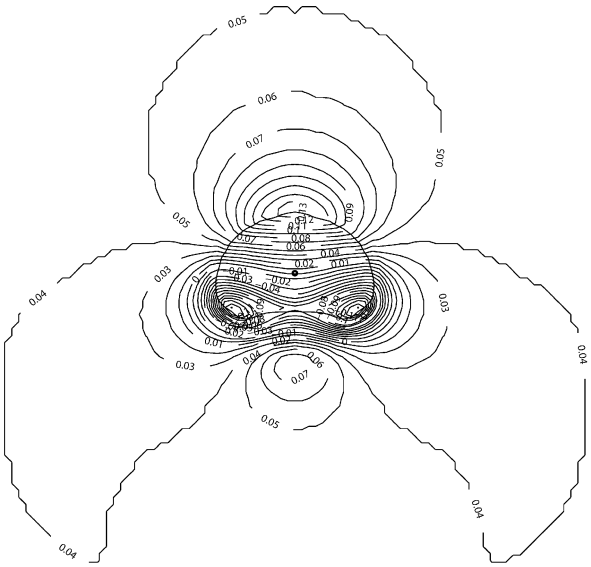


Fig.8. The pressure distribution of $p_{\rm df}$ at $t = 4$ for the case indicated in Fig.7.

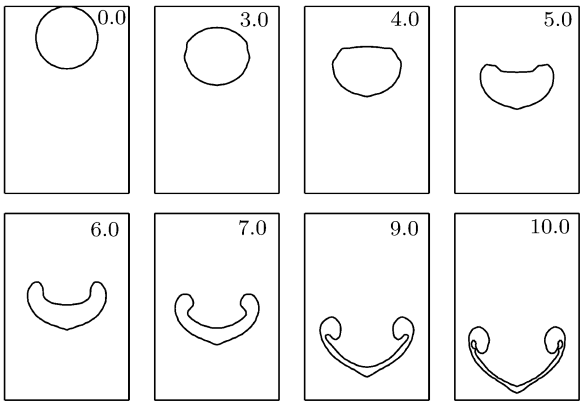


Fig.9. The evolution of a drop with $\lambda = 1.25$, $\mathrm{Re} = \infty$, $\mathrm{We} = \infty$ and $\mathrm{Fr} = 1$.

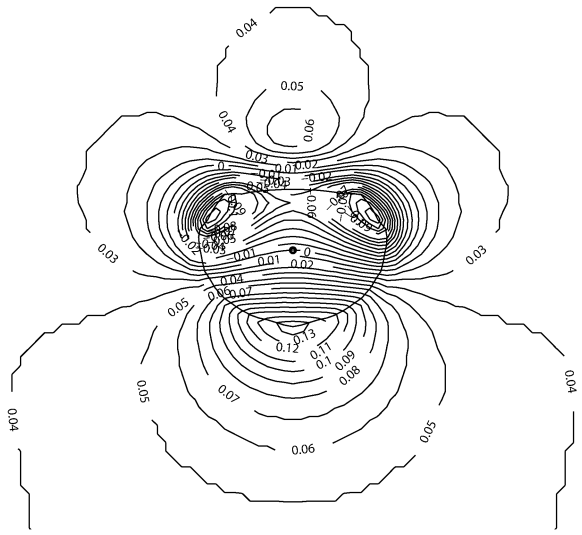


Fig.10. The pressure distribution of $p_{\rm df}$ at $t = 4$ for the case shown in Fig.9.

cause the liquid jet to generate. There is a maximum of $p_{\rm df}$ at lowest point of the drop. The gradient of $p_{\rm df}$ near the maximum point is not large enough to cause a liquid jet to form in front of the drop.

Figure 11 shows the evolution of a drop with $\lambda = 10$, Re $= \infty$, We $= \infty$ and Fr $= 1$. It can be seen that during the early stage of the evolution both the top and bottom of the drop become flatter and flatter, and then a liquid jet forms behind the drop. The jet is very short and wide, and its sideward development is much easier than its forward development because the resistance to deformation at the side parts of the drop is smaller than that at the mid part of the drop due to the much larger fluid density inside the drop than that outside the drop. The development of the jet causes a rolling-up of the drop at the edge of its rear. Finally the drop is broken at its folded-part.

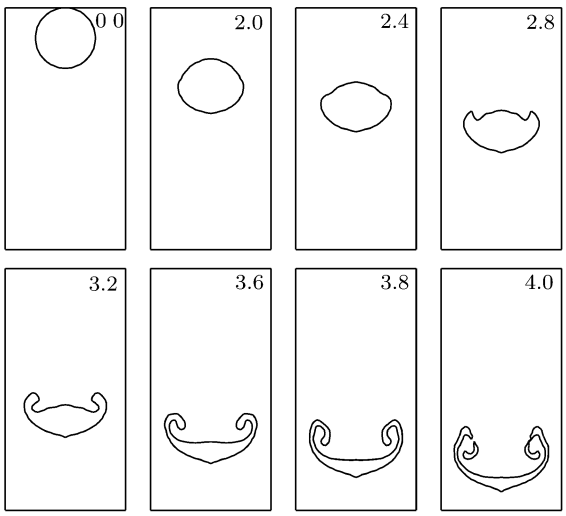


Fig.11. The evolution of a drop with $\lambda = 10$, Re $= \infty$, We $= \infty$ and Fr $= 1$.

4. Conclusion and discussions

A numerical method for simulating the motion and deformation of an axisymmetric bubble or drop rising or falling in another infinite and initially stationary fluid has been developed based on the VOF method in the frame of two incompressible and immiscible viscous fluids under the action of gravity with taking into consideration of surface tension effects. A comparison of the numerical results by this method with those by other works indicates the validity of the method. In the frame of inviscid and incompressible fluids without taking into consideration of surface tension effects, the mechanisms of the generation of the liquid jet and the transition from spherical shape to toroidal shape during the bubble or drop deformation, the increase of the ring diameter of the toroidal bubble or drop and the decrease of its cross-section area during its motion, and the effects of the density ratio on the deformation of the bubble or drop are analysed both theoretically and numerically. Obviously, the numerical method developed in this paper can be applied to the study of the mechanisms of fluid viscosity and surface tension effects on the deformation of bubbles or drops.

References

[1] Zhang A M and Yao X L 2008 *Acta Phys. Sin.* **57** 339 (in Chinese)
[2] Zhang A M and Yao X L 2008 *Chin. Phys.* B **17** 927
[3] Osher S and Fedkiv R P 2001 *J. Comp. Phys.* **169** 463
[4] Liu R X and Shu C W 2003 *Some New Methods in Computational Fluid Dynamics* (in Chinese) (Beijing: Chinese Academic Press) p189–220
[5] Wang F and He F 2006 *Acta Phys. Sin.* **55** 1005 (in Chinese)
[6] Rider W J and Kothe D B 1998 *J. Comp. Phys.* **141** 112
[7] Zou J F, Huang Y Q, Ying X Y and Ren A L 2002 *China Ocean Engnrg.* **16** 525
[8] Bai J S, Li P, Zhang Z J, Hua J S and Tan H 2004 *Chin. Phys.* **13** 1992
[9] Sussman M, Smereka P and Osher S 1994 *J. Comp. Phys.* **114** 146
[10] Walters J K and Davidson J F 1963 *J. Fluid Mech.* **17** 321
[11] Ryskin G and Leal L G 1984 *J. Fluid Mech.* **148** 19
[12] Dandy D S and Leal L G 1989 *J. Fluid Mech.* **208** 161
[13] Lundgren T S and Mansour N N 1991 *J. Fluid Mech.* **224** 177
[14] Sussman M and Smereka P 1997 *J. Fluid Mech.* **341** 269
[15] Huang J T and Zhang H S 2004 *J. Hydrodynamics Ser.* B **16** 379
[16] Batchelor G K 1967 *An Introduction to Fluid Mechanics* (Cambridge: Cambridge University Press) p364–367
[17] Brackbill J U, Kothe D B and Zemach C 1992 *J. Comp. Phys.* **100** 335
[18] Shirani E, Ashgriz N and Mostaghimi J 2005 *J. Comp. Phys.* **203** 154